



Electro-caloric effects in the BaTiO₃-based solid solution ceramics

Bit Chan Kim¹ · Chae Il Cheon¹

Received: 28 February 2020 / Revised: 22 April 2020 / Accepted: 24 April 2020 / Published online: 20 May 2020
© The Korean Ceramic Society 2020

Abstract

Electro-caloric effect (ECE) was investigated in BaTiO₃ (BT)-based solid solution ceramics, Ba(Zr,Ti)O₃ (BZT), Ba(Sn,Ti)O₃ (BST) and (Ba,Ca)(Zr,Ti)O₃ (BCZT) with the composition near an invariant critical point (ICP). The samples were fabricated by the solid-state reaction method and the ECE was obtained by an indirect measurement. The 12BZ–88BT, 9BS–91BT, and 32BCT–68BZT samples showed the best polarization–electric field (P–E) hysteresis characteristics at room temperature and displayed dielectric peaks at 46, 58, and 66 °C, which are the Curie temperatures. With increasing temperature, the P–E loops changed from typical ferroelectric square shapes to paraelectric slanted shapes in the BT-based solid solution ceramics. The adiabatic temperature change due to the ECE (ΔT_{ECE}) showed the maximum values of 0.46 °C at 80 °C, 0.5 °C at 65 °C, and 0.47 °C at 75 °C, respectively, in the 12BZ–88BT, 9BS–91BT, and 32BCT–68BZT samples. The BT-based solid solution ceramics showed smaller maximum ΔT_{ECE} , but broader ΔT_{ECE} peaks at nearer room temperature than the BT ceramic. The enhancement of the ECE due to the multi-phase coexistence was not observed in BT-based solid solutions with the compositions near an invariant critical point (ICP) at which several phases coexist.

Keywords BaTiO₃ · Solid solution · Electro-caloric · Ferroelectric · Ceramics

1 Introduction

The environmental-friendly solid-state cooling devices using caloric materials, which generate (or dissipate) heat by applying (or removing) electric, magnetic or mechanical fields, are expected to replace the current cooling devices which use cyclical compression and expansion of the harmful vapors [1–6]. Electro-caloric effect (ECE) is a change in the temperature of a dielectric material upon the application or withdrawal of an electric field under adiabatic conditions [4–6]. ECE has been observed in many ferroelectric, antiferroelectric, and relaxor materials after a discovery in Rochelle Salt in 1930 but did not attract an attention due to a small temperature change up to recently [6]. In 2006, Mischenko et al. reported a giant ECE with an adiabatic temperature change of about 12 K in antiferroelectric PbZr_{0.95}Ti_{0.05}O₃ thin films by applying a high electric field of 780 kV/cm [7]. This report inspired a research on the ECE again. In recent years, the ECE in Pb-based bulk ceramics have been

reported because the cooling performance in thin film materials is limited due to a small mass [8–15]. Due to a global regulation on the toxic materials, the lead-free electrocaloric materials are being investigated [16–30].

BaTiO₃ (BT) is a typical lead-free ferroelectric material with a first-order phase transition and has been widely applied for many electronic devices such as multilayer capacitors, piezoelectric devices, and temperature sensors [31]. The large ECE was reported in BT single crystals and ceramics [16–19]. Electrocaloric materials for solid-state cooling devices are required to show large ECE in a broad temperature range at near room temperature (RT) [20]. However, the BT single crystals and ceramics displayed the largest ECE at about 130 °C which is higher than room temperature and showed large ECE in narrow temperature range [16–19]. Recently, an adiabatic temperature change due to ECE (ΔT_{ECE}) of 4.5 K over a wide temperature range of 30 K at near RT was obtained in Ba(Zr,Ti)O₃ (BZT) solid solution ceramics with the composition near an invariant critical point (ICP) at which all the four phases (cubic, tetragonal, orthorhombic, and rhombohedral phase) coexist [20]. The large ΔT_{ECE} was explained to ascribe to the large entropy change near ICP due to multi-phase coexistence [20]. However, smaller ECEs ($\Delta T_{ECE} < 0.5$ K) were observed

✉ Chae Il Cheon
cicheon@hoseo.edu

¹ Department of Materials Science and Engineering, Hoseo University, Asan 31499, Chungnam, Korea

in other BT-based solid solution ceramics such as Ba(Sn,Ti)O₃ (BST) and (Ba,Ca)(Zr,Ti)O₃ (BCZT) with the composition near ICP [21, 22]. Different measurement methods for ECE were applied in these reports; a direct measurement using a heat flex sensor in BZT, a direct measurement using modified differential scanning calorimetry in BCZT, and an indirect measurement based on thermodynamic calculation using Maxwell equation in BCZT and BST [20–22]. And the conditions for the fabrication process were not the same in the BT-based ceramics [20–22]. Different measurement methods or different fabrication processes might be the reason for this large difference in ECE of the BT-based solid solution ceramics. Or the ECE may depend largely on the chemical composition in BT-based solid solutions. The assumption that the large ECE is induced in the compositions near ICP by the large dipolar entropy change due to multi-phase coexistence is not clearly confirmed yet, even though the high piezoelectric activities have been reported in BT-based solid solutions with compositions near ICP [32–34].

In this work, ECEs were compared in BT-based solid solution ceramics, BZT, BST, and BCZT with the composition near ICP. The BT-based solid solution ceramics were fabricated by the same solid-state reaction method. The ECEs were obtained in the BT-based solid solutions by an indirect measurement and compared to confirm the assumption that the large ECE is generated in the BT-based solid solution with the compositions near ICP by the large dipolar entropy change due to multi-phase coexistence.

2 Experimental

BT-based solid solution ceramics, Ba(Ti_{1-x}Zr_x)O₃ (*x*BZ), Ba(Ti_{1-x}Sn_x)O₃ (*x*BS), (1-*x*)Ba(Zr_{0.2}Ti_{0.8})O₃-*x*(Ba_{0.7}Ca_{0.3})TiO₃ (*x*BCT), were prepared by a conventional solid oxide reaction method using BaCO₃ (99%, Sigma-Aldrich), CaCO₃ (99%, High Purity Chemicals), TiO₂ (99.9%, High Purity Chemicals), ZrO₂ (99%, Sigma-Aldrich), and SnO₂ (99%, Sigma-Aldrich) as raw materials. The compositions near ICP, which are *x*=0.12, 0.15, 0.18 in *x*BZ, *x*=0.09, 0.11, 0.138 in *x*BS, and *x*=0.27, 0.32, 0.37 in *x*BCT, were investigated in this work.

The raw materials were ball-milled for 24 h in a plastic bottle with ethanol and zirconia balls, and the mixed slurry was dried at 180 °C on a hot plate. The dried powders were calcined at 1250–1350 °C for 2 h. After calcination, the powders were attrition-milled at 350 rpm for 3 h, ball-milled again for 24 h, and dried on a hot plate. The dried powders were granulated by sieving and pressed under 100 MPa in a disk-shaped mold. The compact samples were sintered at 1325–1500 °C for 2 h. The densities of the sintered samples were determined using the Archimedes method. The

crystal structures were examined by X-ray diffraction (XRD, SHIMADZU, Japan). Microstructures were observed with optical microscope (Olympus BX60M, Japan) and scanning electron microscope (SEC, SNE-4500E). For the electric measurements, silver paste was printed on both surfaces of the samples and fired at 800 °C for 10 min. The changes in dielectric properties with temperature were measured in a box furnace at frequencies of 1–1000 kHz using an impedance analyzer (4294A, Agilent). The ferroelectric polarization–electric field (P–E) hysteresis loops were measured at temperatures ranging from RT to 160 °C in silicon oil using a ferroelectric tester (RT66A, Radiant Co., Ltd.) and a high-voltage amplifier (Trek, 609E-6-L-CE, USA). An adiabatic temperature change due to ECE (ΔT_{ECE}) was calculated indirectly using the following thermodynamic Eq. (1) and Maxwell's relation, respectively [5, 6]:

$$\Delta T_{EC} = - \int_{E_1}^{E_2} \frac{T}{\rho C} \cdot \left(\frac{\partial P}{\partial T} \right)_E dE, \quad (1)$$

$$\left(\frac{\partial S}{\partial E} \right)_T = \left(\frac{\partial P}{\partial T} \right)_E, \quad (2)$$

where ρ and C are the density and heat capacity, respectively. The heat capacity of a BaTiO₃ ceramic, which was reported in the literature, was used in the calculation [35]. The polarizations (P) were determined from the upper branches ($E > 0$) of the P–E hysteresis loops measured with a maximum electric field of 2 kV/mm.

3 Results and discussion

Figure 1 shows the changes in the densities of the BT-based solid solution ceramics with increasing the sintering temperature from 1325 to 1500 °C. The densities of BZT and BCZT samples increase abruptly when the sintering temperature increases from 1325 to 1350 °C, and then little change when the sintering temperature further increases from 1350 to 1475 °C. The BST ceramics also show nearly constant densities at the sintering temperatures ranging from 1375 to 1450 °C. Based on the densities and ferroelectric properties, the optimum sintering temperatures are determined to be 1450 °C in BZT and BCZT samples and 1425 °C in BST samples. The following experimental data were collected from the BT-based ceramics sintered at the optimum temperatures. X-ray diffraction patterns of the sintered samples are shown in Fig. 2. All BT-based solid solution ceramics show pseudo-cubic perovskite structures with no impurity phase. It suggests that the lattice distortion from the cubic structure was very small because the compositions of the samples are near ICP.

Figure 3 shows the P–E hysteresis loops of the samples measured at RT. All samples show well-saturated P–E loops. The best P–E hysteresis characteristic with large remanent and saturation polarizations and a small coercive field is observed at 12BZ in BZT and at 9BS in BST samples. The remanent polarizations and the coercive fields of 12BZ and 9BS ceramics are $9.16 \mu\text{C}/\text{cm}^2$, $0.98 \text{ kV}/\text{mm}$ and $8.12 \mu\text{C}/\text{cm}^2$, $0.78 \text{ kV}/\text{mm}$, respectively. The BCZT samples show slightly slanted P–E loops with smaller remanent polarizations than 12BZ and 9BS ceramics as shown in Fig. 3. The

32BCT sample shows the largest remanent polarization and the smallest coercive field in BCZT ceramics, which are $5.63 \mu\text{C}/\text{cm}^2$ and $1.08 \text{ kV}/\text{mm}$, respectively. Temperature-dependent dielectric properties and ECEs were measured in samples with the largest polarization at room temperature, which were 12BZ, 9BS and 32BCT samples.

Figure 4 shows the changes of the dielectric constants with increasing temperature in BT-based solid solution ceramics. The temperature-dependent dielectric constant of the BaTiO_3 ceramic is also displayed in Fig. 4.

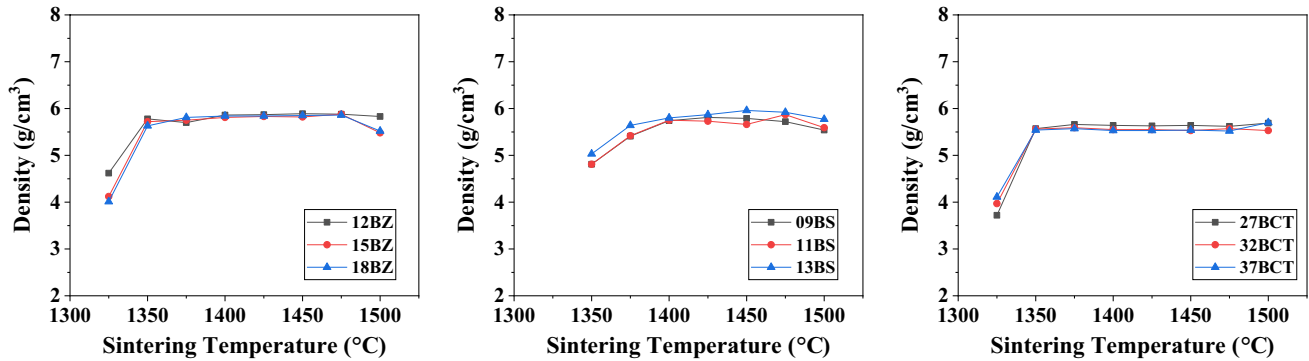


Fig. 1 Changes in the densities of the BT-based solid solution ceramics with increasing the sintering temperature

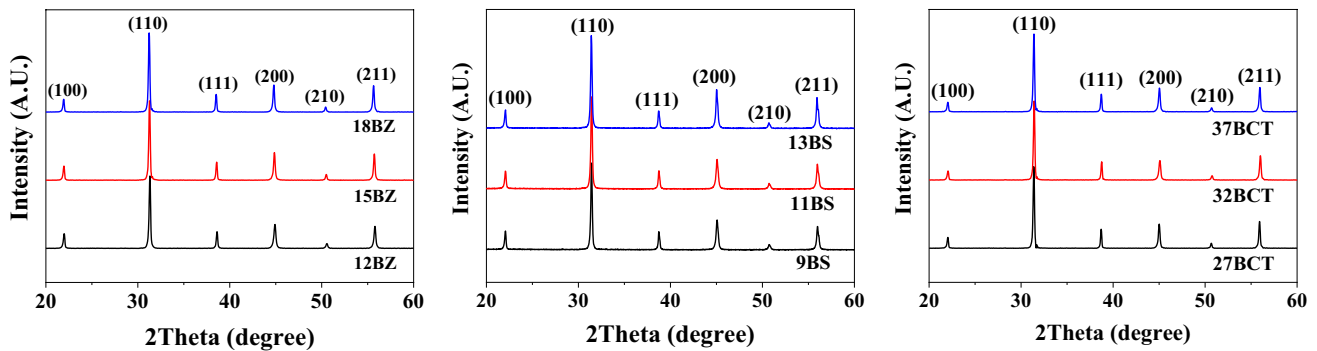


Fig. 2 X-ray diffraction patterns of the BT-based solid solution ceramics sintered at optimized temperature

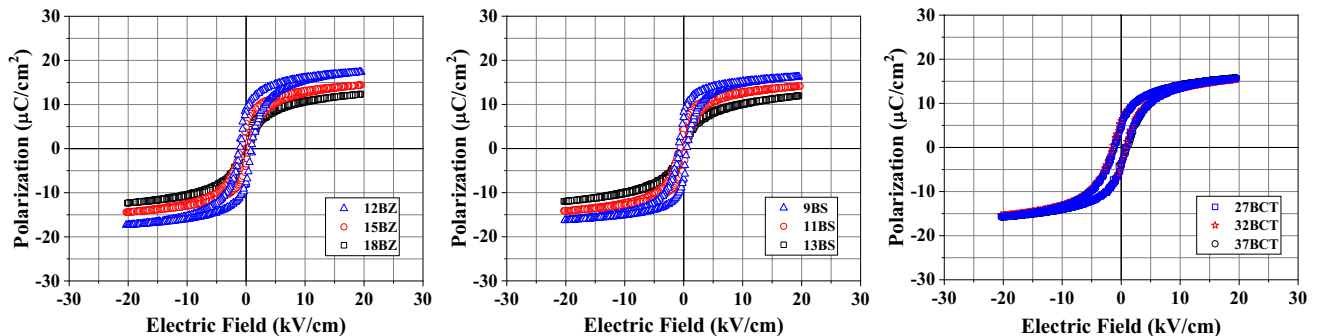


Fig. 3 P–E hysteresis loops of BT-based solid solution ceramics measured at room temperature

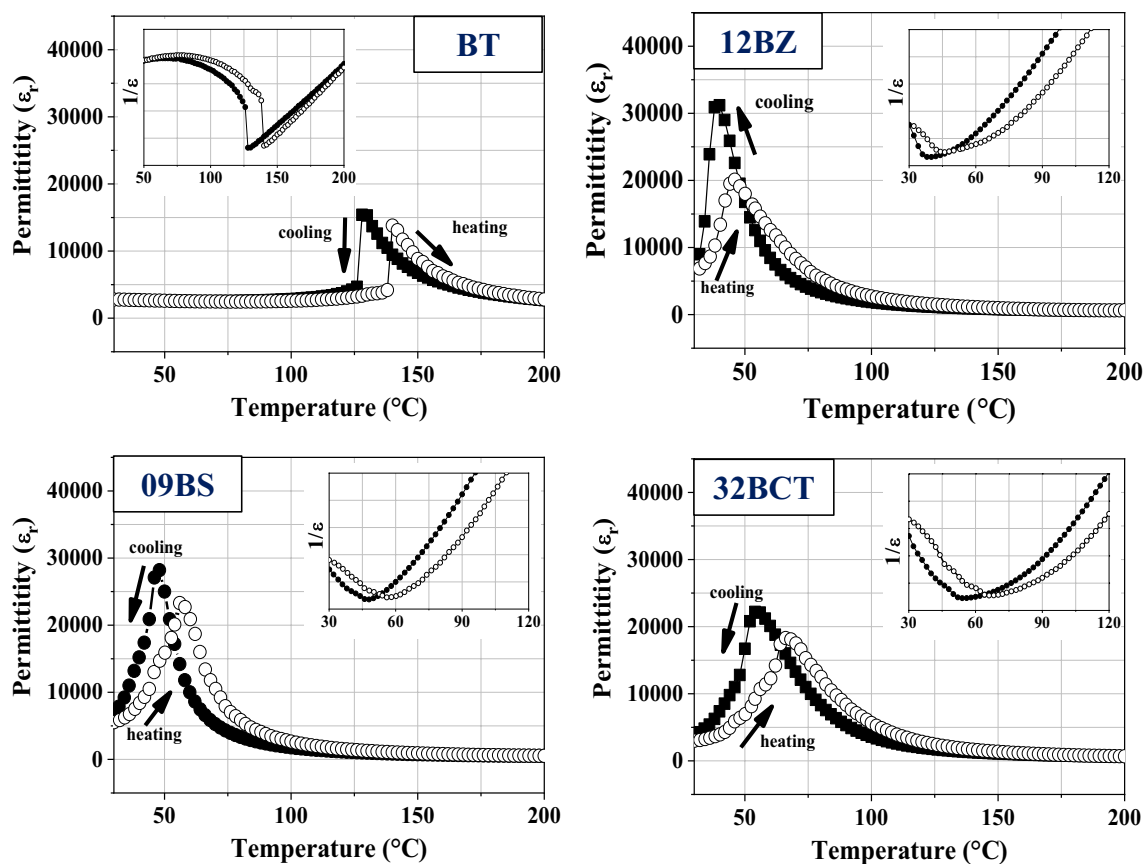


Fig. 4 Temperature-dependent dielectric constants in BT-based solid solution ceramics (Inner graphs are reciprocal dielectric constants)

The dielectric constant of the BaTiO_3 ceramic increases abruptly at 142°C , which is the Curie temperature (T_C), in a heating cycle and shows a peak value at 126°C in a cooling cycle. Thermal hysteresis of the transition temperature is about 16°C . The temperature for the dielectric peak shifts to RT by making solid solutions; the dielectric peaks of BZ, BS, and BCT solid solutions are observed at 46 , 58 , and 66°C in a heating cycle, respectively. The dielectric constant increases more gently from RT to T_C and the thermal hysteresis is reduced in the BT-based solid solutions than in the BT. The inner graphs show the changes in the reciprocal dielectric constant with the temperature. The BT shows the typical dielectric behavior of the ferroelectric material with the first-order phase transition. The discontinuous drop of the reciprocal dielectric constant at T_C which was observed in the BT sample is not shown in the BT-based solid solutions. It indicates that the phase transitions are close to the second order. But the changes in the reciprocal dielectric constants are non-linear in temperatures above T_C . It suggests that the phase transitions are more diffuse than the typical second-order transition from a ferroelectric to a paraelectric phase. Further detail

study is required to understand the phase transition behavior in each BT-based solid solution ceramics clearly.

Figure 5 shows the changes of the P–E hysteresis loops with the increase of the temperature. With increasing temperature, the P–E loops change gradually from typical ferroelectric square shapes to paraelectric slanted shapes and the maximum and the remanent polarizations decrease continuously. The changes in the polarizations at various fields are displayed in Fig. 6. The polarizations at each electric field were determined from the P–E loops measured at various temperatures as shown in Fig. 5. The remanent polarization, the polarization at zero field, decreases quickly when the temperature increases from RT to around T_C . However, the polarization under the electric field decreased gradually from RT to 120°C which is far above T_C . It suggests that the phase transition is more ambiguous under the electric field.

The adiabatic temperature change due to the ECE (ΔT_{ECE}) was obtained in the BT-based solid solutions by an indirect method using Eq. (1). Figure 7 shows that the magnitude of ΔT_{ECE} increases and the temperature for the maximum ΔT_{ECE} ($\Delta T_{\text{ECE, max}}$) shifts to a high temperature with the increase in the applied electric field. The 12BZ,

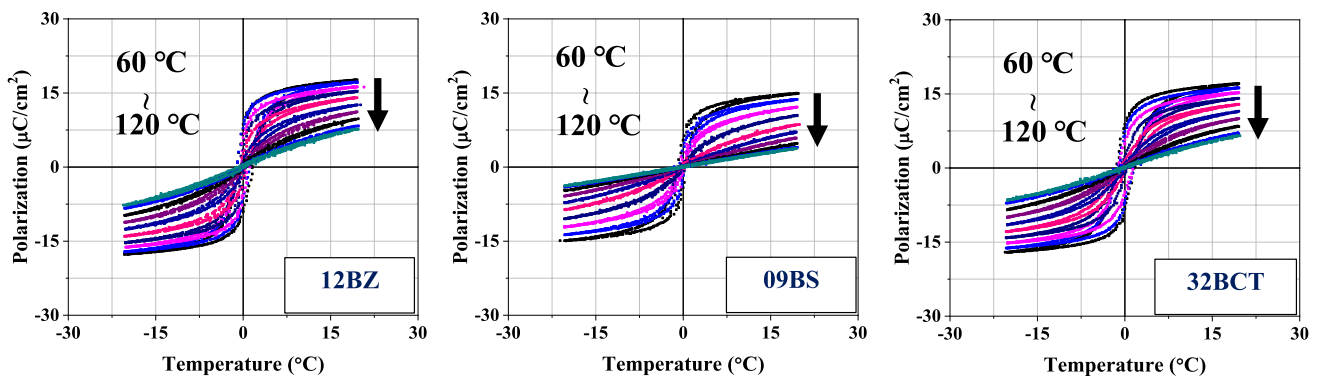


Fig. 5 Changes in P–E hysteresis loops of BT-based solid solution ceramics with increasing temperature

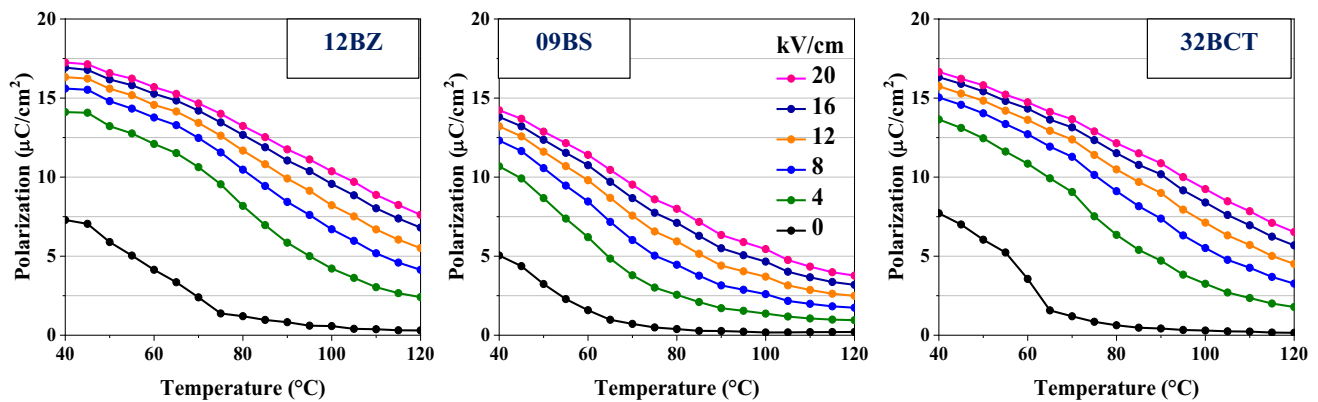


Fig. 6 Changes in polarizations of BT-based solid solutions at various electric fields with increasing temperature

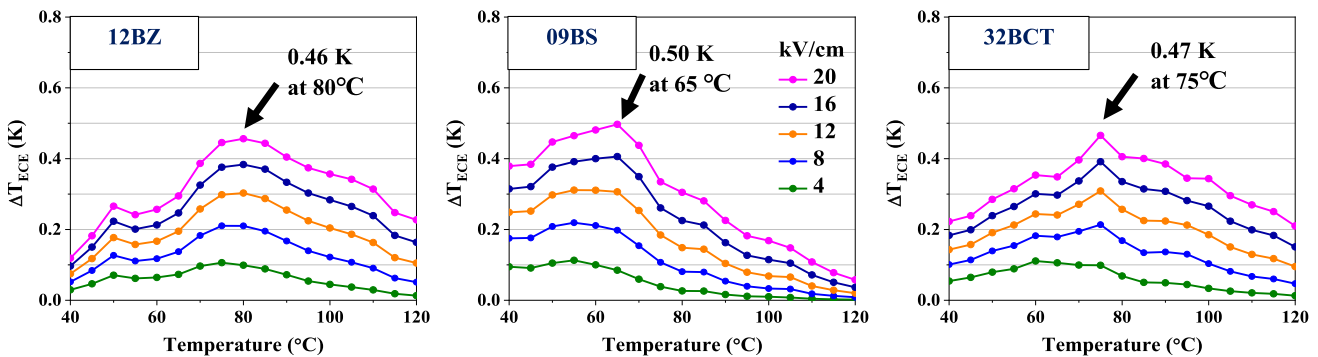


Fig. 7 Changes in the ΔT_{ECE} of BT-based solid solutions at various electric fields with increasing temperature

9BS and 32BCT samples show the $\Delta T_{ECE, \max}$ of 0.46 °C at 80 °C, 0.5 °C at 65 °C, and 0.47 °C at 75 °C, respectively. Recently, the BT ceramic was reported to show the $\Delta T_{ECE, \max}$ of 1.3 °C at 128 °C when an electric field of 2 kV/mm was applied [19]. However, the temperature range to show a large ΔT_{ECE} was very narrow in the BT ceramic [19]. The BT-based solid solution ceramics show smaller $\Delta T_{ECE, \max}$ than the BT ceramic, but display broader ΔT_{ECE}

peak at nearer RT which results from the diffuse phase transition near RT, as shown in Fig. 4. Figure 7 shows that three different BT-based solid solutions, 12BZ, 9BS and 32BCT, have similar $\Delta T_{ECE, \max}$ when the same electric field (2 kV/mm) is applied. The ΔT_{ECE} obtained at various electric fields can be compared by the EC strength which is defined by $|\Delta T_{ECE, \max}|/|\Delta E|$ [16]. The EC strengths of the BT-based solid solutions are displayed in Table 1. The $\Delta T_{ECE, \max}$,

Table 1 Comparison of ECE in BT-based solid solution ceramics

Composition	T (°C)	ΔT_{ECE} (°C)	ΔE (kV/cm)	$ \Delta T_{\text{ECE}}/\Delta E $ (°C•cm/kV)	Method	References
BT	126	1.35	20	0.068	Indirect	[19]
12BZ–88BT	50	0.46	20	0.024	Indirect	This work
20BZ–80BT	69	4.50	150	0.03	Direct	[20]
32BCT–68BZT	50	0.47	20	0.023	Indirect	This work
32BCT–68BZT	76	0.32	20	0.016	Indirect	[22]
32BCT–68BZT	64	0.33	20	0.017	Direct	[22]
09BS–91BT	48	0.5	20	0.025	Indirect	This work
12BS–88BT	45	0.46	20	0.023	Indirect	[21]
35ST–65BT	23	0.42	20	0.021	Indirect	[36]
35ST–65BT	20	3.08	130	0.024	Indirect	[37]

the peak temperature, and the applied electric field are also included in Table 1. The BZT, BST, and BCZT samples in this work had similar EC strengths, 0.023~0.025 Kcm/kV. The reported BZT ceramic with the high $\Delta T_{\text{ECE, max}}$ of 4.5 K shows a EC strength of 0.031 Kcm/kV which is a little higher than those of BZT and other BT-based solid solutions in this work. This result indicates that the very high ΔT_{ECE} reported in the BZT ceramic is not a unique characteristic of the BZT composition but was caused by the high applied electric field. The ECE of the 0.35SrTiO₃–0.65BaTiO₃ (35ST–65BT) ceramic which is one of the BT-based solid solutions with the composition far away from the ICP is included in Table 1. The EC strength of the 35ST–65BT ceramic has been reported to be 0.021~0.023 Kcm/kV which is almost same to those of BT-based solid solutions with the compositions near ICP in this work. It suggests that the composition near ICP is not advantageous to obtain high ECE in the BT-based solid solutions and the multi-phase coexistence does not lead to larger dipolar entropy change.

A very high electric field of 14.5 kV/mm was able to be applied to the BZT ceramics because the samples had very large breakdown strengths probably by the addition of one wt% glass [20]. The very high ΔT_{ECE} of 3.08 K was also obtained by applying a very high electric field of 13 kV/mm in a fully dense 35ST–65BT ceramic which was prepared by spark plasma sintering [37]. The applied electric fields in most reports on the ECE for BT and BT-based solid solutions were 1~2 kV/mm because the P–E hysteresis loops of the BT and BT-based solid solution ceramics were well saturated at the maximum electric field of 1~2 kV/mm. The ECE is expected to be saturated at very high electric field because the increase of the dipolar entropy due to the alignment of electric dipoles would be saturated. The reports on the BZT and ST–BT ceramics indicate that the critical electric field is higher than 13~14.5 kV/mm in BT-based solid solution ceramics. Therefore, the fabrication of the dense ceramic with a very large breakdown strength is required

for obtaining the large ECE in the BT and BT-based solid solutions.

4 Conclusion

X-ray diffraction patterns of BT-based solid solution ceramics with the composition near an invariant critical point (ICP) showed pseudo-cubic perovskite structures at room temperature (RT). The best P–E hysteresis characteristic with the large remanent and saturation polarizations and the small coercive field was observed in 88BT–12BZ, 91BT–9BS, and 32BCT–68BZT samples. The Curie temperatures (T_C) of 88BT–12BZ, 91BT–9BS, and 32BCT–68BZT solid solutions were 46 °C, 58 °C, and 66 °C, respectively. The phase transitions of the BT-based solid solutions were diffuse and close to the second order. With increasing temperature, the P–E loops changed from typical ferroelectric square-shapes to paraelectric slanted shapes. The remanent polarization decreased quickly when the temperature increased from RT to around T_C , while the polarization under the electric field decreased gradually from RT to 120 °C which is far above T_C . The adiabatic temperature change due to the ECE (ΔT_{ECE}) was obtained in the BT-based solid solutions by an indirect method. The 88BT–12BZ, 91BT–9BS, and 32BCT–68BZT samples showed the maximum ΔT_{ECE} of 0.46 °C at 80 °C, 0.5 °C at 65 °C, and 0.47 °C at 75 °C, respectively. The BT-based solid solution ceramics showed smaller maximum ΔT_{ECE} , but broader ΔT_{ECE} peak at nearer RT than the BT ceramic. Three different BT-based solid solutions, 88BT–12BZ, 91BT–9BS, and 32BCT–68BZT, had similar EC strengths ($|\Delta T_{\text{ECE, max}}|/|\Delta E|$) of 0.023~0.025 Kcm/kV. The very high ECEs reported in some BT-based solid solutions were not caused by larger dipolar entropy change of the composition near ICP due to the multi-phase coexistence but resulted from the high applied electric field in samples with very large breakdown strengths.

Acknowledgements This study was supported by the Basic Science Research Program through the National Research Foundation of Korea (NRF), funded by the Ministry of Education (NRF-2017R1D1A1B03031257).

References

1. E. Defay, R. Faye, G. Despesse, H. Strozyk, D. Sette, S. Crossley, X. Moya, N.D. Mathur, *Nat. Commun.* **9**, 1827 (2018)
2. X. Moya, E. Defay, V. Heine, N.D. Mathur, *Nat. Phys.* **11**, 202 (2015)
3. X. Moya, S. Kar-Narayan, N.D. Mathur, *Nat. Mater.* **13**, 439 (2013)
4. S. Crossley, N.D. Mathur, X. Moya, *AIP Adv.* **5**, 067153 (2015)
5. J.F. Scott, *Annu. Rev. Mater. Res.* **41**, 229 (2011)
6. Y. Liu, J.F. Scott, B. Dkhil, *Appl. Phys. Rev.* **3**, 031102 (2016)
7. A.S. Mischenko, Q. Zhang, J.F. Scott, R.W. Whatmore, N.D. Mathur, *Science* **311**, 1270 (2006)
8. B. Rozic, M. Kosec, H. Ursic, J. Holc, B. Malic, Q.M. Zhang, R. Blinc, R. Pirc, Z. Kutnjak, *J. Appl. Phys.* **110**, 064118 (2011)
9. F.L. Goupil, A. Berenov, A.-K. Axelsson, M. Valant, N.M. Alford, *J. Appl. Phys.* **111**, 124109 (2012)
10. J. Perantie, H.N. Taylor, J. Hagberg, H. Jantunen, Z.-G. Ye, *J. Appl. Phys.* **114**, 174105 (2013)
11. J. Perantie, J. Hagberg, A. Uusimaki, H. Jantunen, *Phys. Rev. B* **82**, 134119 (2010)
12. J. Li, S. Qin, Y. Bai, J. Li, L. Qiao, *Appl. Phys. Lett.* **111**, 093901 (2017)
13. B. Lu, P. Li, Z. Tang, Y. Yao, X. Gao, W. Kleemann, S.G. Lu, *Sci. Rep.* **7**, 45335 (2017)
14. F. Zhuo, Q. Li, H. Qiao, Q. Yan, Y. Zhang, X. Xi, X. Chu, X. Long, W. Cao, *Appl. Phys. Lett.* **112**, 133901 (2018)
15. L. Fulanovic, S. Drnovsek, H. Ursic, M. Vrabelj, D. Kuscer, K. Makarovic, V. Bobnar, Z. Kutnjak, B. Malic, *J. Euro. Ceram. Soc.* **37**, 599 (2017)
16. X. Moya, E. Stern-Taulats, S. Crossley, D. Gonzalez-Alonso, S. Kar-Narayan, A. Planes, L. Manosa, N.D. Mathur, *Adv. Mater.* **25**, 1360 (2013)
17. Y. Bai, X. Han, X.-C. Zheng, L. Qiao, *Sci. Rep.* **3**, 2895 (2013)
18. X.-C. Ren, W.-L. Nie, Y. Bai, L.-J. Qiao, *Eur. Phys. J. B* **88**, 232 (2015)
19. B.C. Kim, K.W. Chae, C.I. Cheon, *J. Korean Phys. Soc.* **76**, 226 (2020)
20. X.-S. Qian, H.-J. Ye, Y.-T. Zhang, H. Gu, X. Li, C.A. Randall, Q.M. Zhang, *Adv. Funct. Mater.* **24**, 1300 (2014)
21. X. Zhang, L. Wu, S. Gao, J.Q. Liu, B. Xu, Y.D. Xia, J. Yin, Z.G. Liu, *AIP Adv.* **5**, 047134 (2015)
22. M. Sanlialp, V.V. Shvartsman, M. Acosta, D.C. Lupascu, *J. Am. Ceram. Soc.* **99**, 4022 (2016)
23. D.S. Kim, B.C. Kim, S.H. Han, H.-W. Kang, J.S. Kim, C.I. Cheon, *J. Appl. Phys.* **126**, 234101 (2019)
24. M. Zannen, A. Lahmar, B. Asbeni, H. Khemakhem, M.E. Marssi, Z. Kutnjak, M.E. Souni, *Appl. Phys. Lett.* **107**, 032905 (2015)
25. Z. Fan, X. Liu, X. Tan, *J. Am. Ceram. Soc.* **100**, 2088 (2018)
26. L. Li, M. Xu, Q. Zhang, P. Chen, N. Wang, D. Xiong, *Ceram. Int.* **44**, 343 (2018)
27. W.P. Cao, W.L. Li, X.F. Dai, T.D. Zhang, J. Sheng, Y.F. Hou, W.D. Fei, *J. Euro. Ceram. Soc.* **36**, 593 (2016)
28. F.L. Goupil, N.M. Alford, *APL Mater.* **4**, 064104 (2016)
29. F. Li, G. Chen, X. Liu, J. Zhai, B. Shen, H. Zeng, S. Li, P. Li, K. Yang, H. Yan, *J. Euro. Ceram. Soc.* **37**, 4732 (2017)
30. E. Birks, M. Duncie, J. Perantie, J. Hagberg, *J. Appl. Phys.* **121**, 224102 (2017)
31. M. Acosta, N. Novak, V. Rojas, S. Patel, R. Vaish, J. Koruza, G.A. Rossetti, J. Rödel, *Appl. Phys. Rev.* **4**, 041305 (2017)
32. W. Liu, X. Ren, *Phys. Rev. Lett.* **103**, 257602 (2009)
33. Z. Yu, C. Ang, R. Guo, A.S. Bhalla, *J. Appl. Phys.* **92**, 1489 (2002)
34. Y. Yao, C. Zhou, D. Lv, D. Wang, H. Wu, Y. Yang, X. Ren, *Europhys. Lett.* **98**, 27008 (2012)
35. Y. He, *Thermochim. Acta* **419**, 135 (2004)
36. Y. Bai, X. Han, K. Ding, L.-J. Qiao, *Appl. Phys. Lett.* **103**, 162902 (2013)
37. X. Qiang, T.T. Chen, Y.J. Wu, X.M. Chen, *J. Am. Ceram. Soc.* **94**, 1021 (2013)

Publisher's Note Springer Nature remains neutral with regard to jurisdictional claims in published maps and institutional affiliations.